

CIGS Mini-Modules with Dispensed Metallization on Transparent Conductive Oxide Layer

Katharina Gensowski,* Ana Jimenez, Timo Freund, Noah Wengenmeyr, Sebastian Tepner, Maximilian Pospischil, and Florian Clement

This article presents the application of a parallel dispensing device for low-temperature silver paste metallization on transparent conductive oxide (TCO) layers of $\text{Cu}(\text{In}_{1-x}\text{Ga}_x)\text{Se}_2$ (CIGS) substrates as an alternative metallization technology to screen printing and inkjet printing. A curing variation experiment is performed to analyze the effect of different curing conditions on the resulting contact resistivity of the metal grid. Contact resistivity values below $5 \text{ m}\Omega\text{cm}^2$ are achieved. Furthermore, CIGS mini-modules are metallized with three different low-temperature paste formulations obtaining a record core finger geometry of $25 \mu\text{m}$ and an average optical aspect ratio of 0.46 using $25 \mu\text{m}$ nozzle openings. The dispensed metal grid on the TCO layers achieves the comparable current density values of $j_{\text{sc}} = 32.2 \text{ mA cm}^{-2}$ and the open-circuit voltages values per cell of $V_{\text{oc}} = 672 \text{ mV}$ as the screen printed metal grid on CIGS mini-modules and, hence, a nominal power of 2.05 W. The metal grid enables the use of broader cell widths compared with grid-free CIGS samples and results in a reduced dead area.

1. Introduction

Thin-film technologies, especially $\text{Cu}(\text{In}_{1-x}\text{Ga}_x)\text{Se}_2$ (CIGS) thin-film solar cells, have a high efficiency potential. CIGS has become one of the most competitive thin-film technologies regarding efficiency and economics to silicon photovoltaics (PV).^[1–4] The CIGS cell record efficiency of 23.35% has been presented in 2019 by Solar Frontier (cell area: 1 cm^2).^[5] Later that year, NICE Solar Energy GmbH obtained a new CIGS module record of 17.6% on a module area of $1.20 \times 0.60 \text{ m}^2$.^[6] However, the annual global production of CIGS thin-film modules is still relatively low compared with conventional PV production with less than 2000 MWp in 2017.^[7] One reason for this low market share is the efficiency gap between cell and module level with up to 8% abs. between the CIGS cell record and commercial


modules. In comparison with that, the efficiency gap between cell and module for crystalline silicon PV is only 4% abs.^[8]

Bermudez and Perez-Rodriguez summarized the reasons for the cell-to-module gap, which occurs in all PV technologies but in different scales.^[8] In silicon PV, the main cell to module efficiency loss appears because of resistive losses introduced by the interconnection technology. In addition, for the CIGS technology, further efficiency is lost because of lateral inhomogeneity in the functional CIGS layer deposition, especially when the upscaling process from square centimeter to square meter area is considered. These inhomogeneities decrease the open-circuit voltage and further influence the bandgap of the CIGS absorbers.^[9–11] The different modularization strategies are an additional

reason of this huge CIGS cell-to-module gap. Typically, the P1P2P3 monolithic interconnection is used, which allows a sequential interconnection during the CIGS cell manufacture procedure.^[3,12,13] Here, cell widths as well as the scribing widths define the dead area and, therefore, further contribution to efficiency losses in modules. Besides that, three promising ways to decrease the CIGS cell-to-module gap are discussed in the previous study^[8] 1) new transparent conductive oxides (TCOs) including improved deposition methods;^[14–17] 2) hybrid modularization approaches, which combine the standard P1P2P3 scribing and applying a metal grid on the TCO; and 3) use of wide-bandgap solar absorbers.^[17–21] Further approaches to optimizing module performance are reported in the previous studies.^[22,23] This work focuses on the promising approach of hybrid modularization. The manufacturing procedure of silicon solar cells includes the application of a metal grid as a standard process step. This idea is transferred to the hybrid modularization approaches for the CIGS thin-film technology. The metal grid ensures a decrease of resistive losses by minimizing the impact of front contact.^[24] Consequently, larger cell areas are applicable, causing a reduction of scribed cell interconnections per module, which reduces module voltage as well as total dead area and, thus, increases short circuit current and fill factor (FF). On a system level, a reduction of module voltage while simultaneously increasing the current is the key to further reduce the high balance of system (BOS) costs of CIGS. In addition, the laser processes for scribing are constantly improved, resulting in narrower scribing widths and less scribing-induced damages.

K. Gensowski, A. Jimenez, N. Wengenmeyr, S. Tepner, Dr. M. Pospischil, Dr. F. Clement
 Fraunhofer Institute for Solar Energy Systems
 Heidenhofstraße 2, 79110 Freiburg im Breisgau, Germany
 E-mail: katharina.gensowski@ise.fraunhofer.de

T. Freund
 NICE Solar Energy GmbH
 Alfred-Leikam-Straße 25, 74523 Schwäbisch Hall, Germany

 The ORCID identification number(s) for the author(s) of this article can be found under <https://doi.org/10.1002/solr.202000475>.

DOI: 10.1002/solr.202000475

To date, the state-of-the-art approaches to apply the metal grid are flatbed screen printing (SP) or inkjet printing.^[25,26] Several publications show different hybrid modularization approaches partly using the inkjet technology to apply dielectric and conductive inks.^[27–33] These printing technologies are able to achieve competitive throughputs with a proven track record of industrial application in numerous sectors. The dispensing (DIS) approach is an alternative promising printing technology to SP and inkjet printing to apply the metal grid on TCO surfaces. Here, commercial high viscous silver SP pastes are extruded through narrow nozzle openings in the range of 20–60 μm . Results for dispensed metal grids on different silicon solar cell concepts have been presented with high- and low-temperature pastes, demonstrating narrow contact fingers below 20 μm .^[34–36]

In this study, we present screen printed and dispensed metal grids on 156 mm \times 156 mm transfer length method (TLM) CIGS substrates and 156 mm \times 156 mm CIGS mini-modules (total area). Our experimental plan focuses on the comparison of the DIS technology to an SP reference. Three different low-temperature silver pastes are applied, and the curing conditions are varied in a temperature range from 170 to 200 $^{\circ}\text{C}$. The electrical performance of the CIGS substrates is characterized and correlated with finger geometries of the printed metal gridlines.

2. Overview on Printing Technologies for Metallization of CIGS Substrates

2.1. Flatbed Screen Printing

During the last two decades, the widths of printed structures in flatbed SP have been significantly reduced for silicon PV.^[37,38] To date, this industrially widespread technology dominates the PV metallization market.^[39] The SP process mechanics of highly filled suspensions, e.g., metal pastes, are well described in the literature.^[40,41] The paste is pushed over a screen by an angled

squeegee, creating a downward velocity component into the mesh with its opened and closed areas (flooding). Afterwards, the second squeegee with a controlled vertical force creates a moving contact line between the screen and substrate. Once the pressure releases the screen snaps off and leaves behind the printed structure. In the case of metallization of CIGS modules, the screen has a huge area (active printing area: 60 cm \times 120 cm), limiting the screen stability and causing significant screen distortion. Furthermore, a large paste volume is required, which is permanently in contact with the environment. Mesh marks are shown in the printed structure, resulting in inhomogeneity of finger height and, thus, non-optimal silver consumption (see Figure 1).

2.2. Dispensing Technology

The DIS technology is an established industrial technology in different industrial sectors, but not yet for metallization in PV.^[35,36,42,43] Fraunhofer Institute for Solar Energy Systems (ISE) developed the method and apparatus for DIS metal grids for solar cell applications and works constantly on improving the DIS technology for over more than ten years.^[36,44,45] The metal paste is extruded through narrow openings smaller than 60 μm , either single nozzles or print heads with up to 130 nozzle openings are used, whereby multinozzle print heads are normally used to obtain the industrial needed throughput.^[36] In 2019, the Fraunhofer spin-off HighLine Technology GmbH was founded with the goal to commercialize a multinozzle print head for the parallel DIS technology.^[46] The paste reservoir is a closed system to prevent paste drying.^[47] Depending on the desired structure width, the nozzle diameters are chosen. Similar to inkjet printing, the DIS technology is also a direct writing process. The extruded paste threads or paste dots are printed onto the substrate surface. Here, only the paste gets in contact with the substrate. To achieve homogeneous printing results, a constant

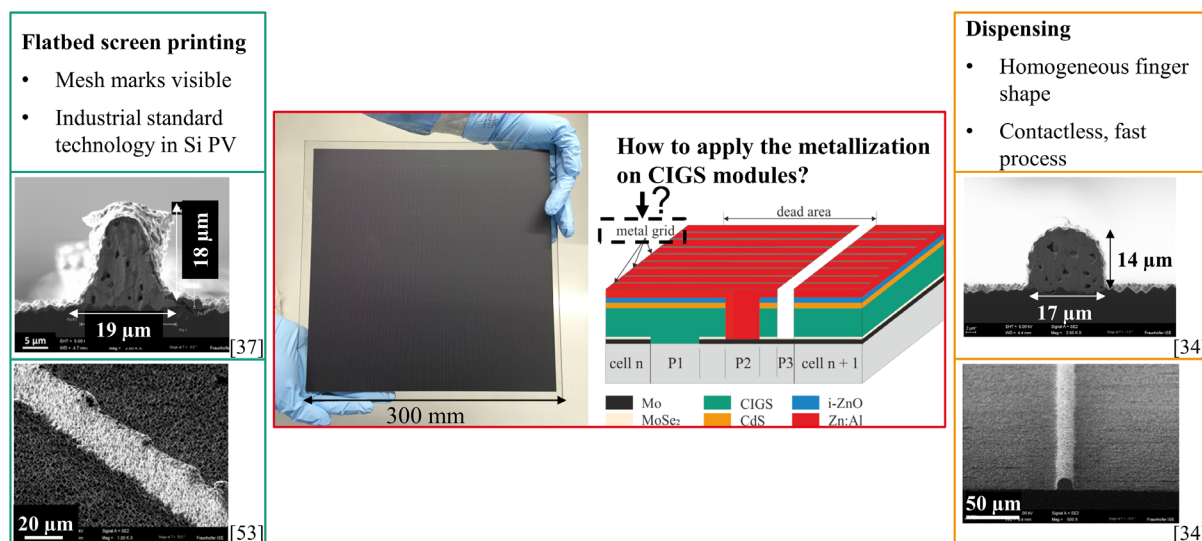


Figure 1. Overview on possible printing technologies for metallization of CIGS modules. Respective world record contact shapes applied by flat SP and DIS technology are shown. These silver pastes are printed on different solar cell substrates. The questions are how the performances of those printing technologies on CIGS substrates compare and which advantage each approach has.^[34,37,53]

DIS gap between the nozzle openings and the substrate is required. However, in case of metallization CIGS substrates, the DIS approach shows an advantage regarding the variable thickness deviation of the glass substrate caused by melting during the CIGS deposition. Different solutions are imaginable to realize homogeneous metal grids. In addition, the DIS process has no limits in upscaling of large CIGS module areas. The requirements for the printing pastes are similar to SP paste, allowing to use the same commercial products applied to silicon heterojunction approaches without the need for additional adaptations.^[48] Nowadays, paste manufacturers started to do minor adjustments of SP paste formulations to further optimize process stability and finger geometry of dispensed structures.^[48]

3. Experimental Section

Figure 2 shows all the experimental work of our study with respect to application tests of low-temperature silver pastes on CIGS substrates and the characterization of their electrical performance. In the first experiment, different curing conditions of three low-temperature silver pastes are analyzed regarding their contact resistivity $\rho_{c,TLM}$ and sheet resistance $R_{sh,TLM}$. The curing temperature and duration are varied between $T_c = 170^\circ\text{C}$ and $T_c = 200^\circ\text{C}$ and from $t_c = 5\text{ min}$ to $t_c = 20\text{ min}$, respectively. All pastes are applied by the DIS approach. Based on these results, the curing conditions for the second experiment “Application of metal grid on CIGS substrates” are chosen. This second experimental plan consists of 15 different groups

(see Figure 2). Depending on the experimental group, CIGS TLM substrates or CIGS mini-modules are used. Five CIGS TLM substrates per group and ten CIGS mini-modules per group are processed. Group 0 is the reference group without grid on the TCO layer with a cell width of 4.07 mm, and the CIGS mini-modules consist of 29 cells. Three low-temperature silver pastes are applied by the DIS technology; in addition, paste A is also disposed by SP (groups 1–4). Two promising curing conditions of the pretest are performed on TLM substrates and mini-modules for pastes A and B, and one curing condition of the pretest is used for paste sample C. The printed metal grids are characterized regarding their contact finger geometry and their electrical performance. The contact resistivity $\rho_{c,TLM}$ as well as the sheet resistance $R_{sh,TLM}$ are measured by the TLM method. For all CIGS mini-modules, $I-V$ measurements are conducted.

The applied low-temperature silver pastes A and B are commercially available SP pastes for silicon heterojunction solar cell metallization, and paste C is a specially adjusted paste for DIS application. These paste formulations are highly filled suspensions, which have a shear viscosity in the range of 600–700 mPas at the speed of a rotation of 5 rpm. The nonvolatile content of the three pastes is between 91% and 93% after curing. We used the CIGS samples from our project partner NICE Solar Energy GmbH. The stacking sequence Mo/CIGS/chemical bath deposition (CBD)-CdS/i-ZnO/ZnO:Al/indium tin oxide (ITO) is deposited on a 3 mm thick glass substrate, beginning with the rear contact material molybdenum, as described in the literature.^[49,50] Then, the CIGS layer is applied by co-evaporation of copper, indium, and gallium in a selenium containing atmosphere

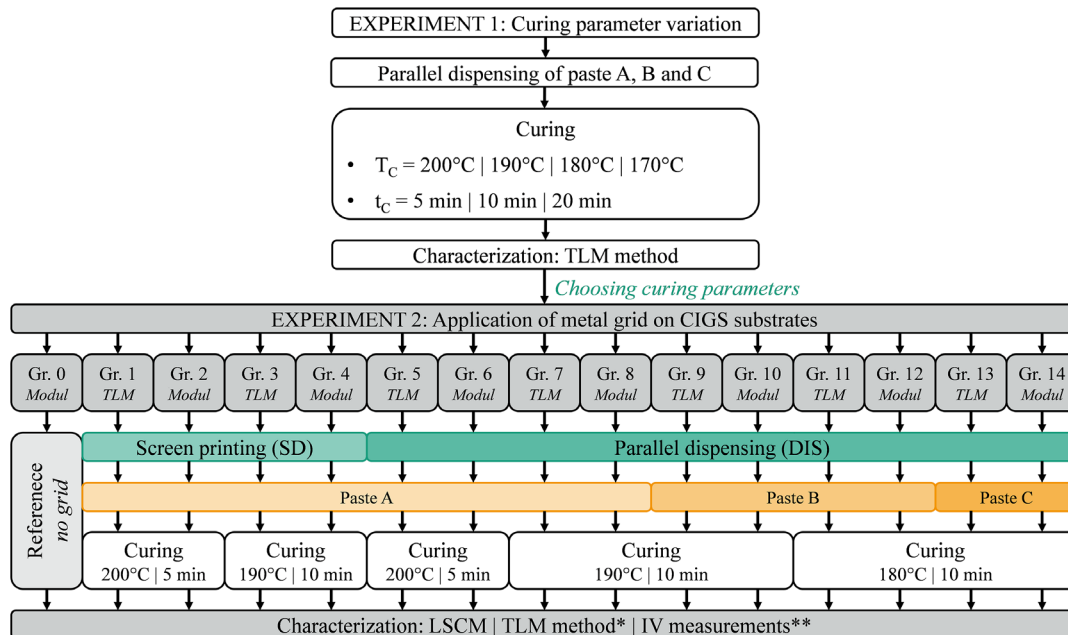


Figure 2. Overview of all investigated experiments for the presented study. On top, the preliminary test shows the curing variations of three low-temperature silver pastes within the temperature range of $T_c = 170\text{--}200^\circ\text{C}$ applied by DIS. The curing duration varies from $t_c = 5\text{ min}$ to $t_c = 20\text{ min}$. Characterization is done by the TLM method to measure the contact resistivity $\rho_{c,TLM}$ and the sheet resistance $R_{sh,TLM}$. The results are used for further experiments. Subsequently, SP of paste A (groups 1–4) and DIS of pastes A–C are applied on CIGS TLM substrates and on CIGS mini-modules (groups 5–14) (cell width: 6.94 mm). Group 0 is the reference group including grid-free CIGS mini-modules (cell width: 4.07 mm). The printed contact fingers are characterized regarding their finger geometry by a 3D confocal laser scanning microscope (CLSM) and their electrical performance (* CIGS TLM substrates and ** CIGS mini-modules).

(without alkali post-deposition treatment). Subsequently, the buffer layer CdS is deposited using CBD. An ITO is applied on CIGS substrates, which are metallized to realize a better contact resistance on the ZnO:Al layer (groups 1–14). The P1 scribing is realized by the laser process, and the P2 and P3 scribing is done mechanically. The CIGS TLM substrates have a size of 156 mm × 156 mm and show no P1P2P3 patterning. The active area of the CIGS mini-modules is 137.43 cm² (with a cell width of 6.94 mm) onto a 156 mm × 156 mm glass substrate with a thickness of 3 mm. One mini-module consists of 17 cells in total.

3.1. Metallization of CIGS Substrates

A semi-automatic screen printer EKRA XH STS and a screen with the screen openings of $w_n = 40 \mu\text{m}$ are used to apply the screen printed grid of groups 1–4. The disposed calendered mesh has a specification of $360 \times 0.016 \times 22.5^\circ$ with an emulsion over mesh (EOM) of EOM = 15 μm . The printing speed is $v_{\text{squeegee}} = 100 \text{ mm s}^{-1}$ onto CIGS TLM substrates and mini-modules.

All parallel DIS experiments are realized with a DIS platform from ASYS GmbH, Germany: Here, CIGS substrates are placed individually on a vacuum chuck. An R&D print head, so called “GECKO,”^[42] with different nozzle openings is integrated into the ASYS platform. Ten runs of the GECKO print head are needed to dispense the metal grid across the whole sample. Paste A is dispensed through 35 μm nozzle openings with a DIS velocity of $v_{\text{disp}} = 100 \text{ mm s}^{-1}$. This paste formulation is dispensed at a temperature of $T_{\text{disp}} = 5^\circ\text{C}$. For pastes B and C, the nozzle openings of 25 μm are used. Paste B is dispensed with a printing speed of $v_{\text{disp}} = 60 \text{ mm s}^{-1}$ and paste C with a DIS velocity of $v_{\text{disp}} = 160 \text{ mm s}^{-1}$. Pastes B and C are heated to a temperature of $T_{\text{disp}} = 25^\circ\text{C}$ for the DIS approach. The DIS gap between the nozzles and the substrate is 600 μm for all DIS experiments.

Subsequently, the metallized CIGS samples are cured in the convection oven R0400FC from Essemtec AG, Switzerland. Before starting the curing process, the oven is preheated at least 30 min to guarantee a homogeneous temperature distribution. The curing temperatures vary between $T_c = 170^\circ\text{C}$ and $T_c = 200^\circ\text{C}$ with a curing duration between $t_c = 5 \text{ min}$ and $t_c = 20 \text{ min}$ for the preliminary experiment. Depending on the applied low-temperature paste, the curing temperature varies between $T_c = 180^\circ\text{C}$ and $T_c = 200^\circ\text{C}$ for experiment 2. The curing duration is either $t_c = 5 \text{ min}$ or $t_c = 10 \text{ min}$ (see Figure 2).

3.2. Characterization Methods

3.2.1. Geometric Analysis of Printed Contact Fingers

The printed contact fingers are measured using the commercially available 3D CLSM OLS4000 from OLYMPUS with a magnification of 50. Nine segments with a length of 1.5 mm are measured for each TLM group of the experimental plan. The geometric parameters are identified by software, developed by Fraunhofer ISE.^[51] The procedure and definition of parameters are well described in the literature.^[36] The finger width w_{shading} describes the shaded area of the finger including any spreading.

In addition, the core finger width w_{core} , the finger height $h_{f,\text{max}}$, and the cross-sectional area A_{cross} are determined. The electrical and optical aspect ratio AR_{el} and AR_o and, further, the spreading coefficient $\xi_{\text{spreading}}$ are calculated (see Equation (1)–(3)). The spreading coefficient $\xi_{\text{spreading}}$ describes the ratio of the finger width w_{core} to the finger width w_{shading} .^[36,52]

$$AR_o = \frac{h_{f,\text{max}}}{w_{\text{shading}}} \quad (1)$$

$$AR_{\text{el}} = \frac{h_{f,\text{avg}}}{w_{\text{shading}}} = \frac{A_{\text{cross}}}{w_{\text{shading}}^2} \quad (2)$$

$$\xi_{\text{spreading}} = \frac{w_{\text{core}}}{w_{\text{shading}}} \quad (3)$$

3.2.2. Electrical Characterization

The contact resistivity $\rho_{c,\text{TLM}}$ and the sheet resistance $R_{\text{sh,TLM}}$ of TCO are determined by TLM Scan from pv-tools GmbH. The 156 mm × 156 mm CIGS TLM substrates are separated into 10 mm wide stripes. In total, 14 stripes per substrate are investigated by TLM characterization with at least 150 measurements for each sample. For the TLM characterization, a measuring head consisting of eight measuring tip pairs is precisely arranged onto the contact grid. A measuring current of $I = 10 \text{ mA}$ is applied.

The electrical parameters of CIGS mini-modules are determined by h.a.l.m flasher IV tool at standard test conditions. The CIGS mini-modules are prepared for the measurement as follows: after the P1 and P2 scribing, the metallization is applied on the TCO layer, and subsequently, the P3 structuring is realized mechanically. Hence, the P2 structures of the metallized CIGS mini-modules contain the TCO material and metal paste, whereas the P2 structures of the grid-free CIGS mini-modules include only the TCO layer. Contact stripes are fixed in a laminator at a temperature of $T = 130^\circ\text{C}$. The I – V measurements are done with the non-laminated modules at 1000 W m^{-2} .

4. Results and Discussion

4.1. Comparison between Screen Printed and Dispensed Finger Geometry

Figure 3 shows the microscope images of finger geometries on CIGS substrates of the two printing technologies, SP versus DIS, and three applied pastes. In the first column of the illustration, a representative screen printed contact finger of paste A is shown (groups 1 and 3). This microscope image shows a contact finger section of 1.5 mm, and the mesh marks are clearly visible in the printed structure. The finger width is $w_{\text{shading}} = 55 \pm 2 \mu\text{m}$, and the average optical aspect ratio is $AR_o = 0.35 \pm 0.03$ ($AR_{\text{el}} = 0.21 \pm 0.02$). Dispensed contact fingers have a constant height profile compared with screen printed fingers, which results in a more effective silver consumption regarding the electrical conductivity. DIS paste A results in an average finger width of $w_{\text{shading}} = 46 \pm 3 \mu\text{m}$. The optical aspect ratio is $AR_o = 0.38 \pm 0.02$ ($AR_{\text{el}} = 0.26 \pm 0.03$). The finger geometries

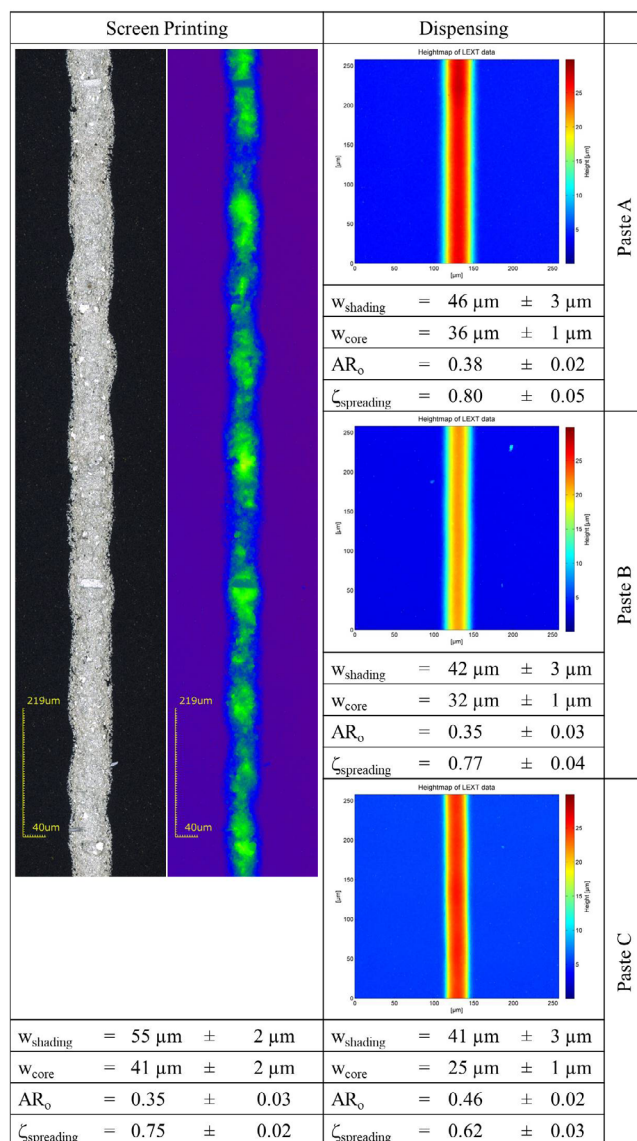


Figure 3. Analysis of the finger geometry of the printed contact fingers of pastes A–C. All finger geometries are characterized with CLSM at a magnitude rate of 50 (see Section 3.2.1.). On the left, the microscope picture of a screen printed contact finger is shown. The finger width is $w_{\text{shading}} = 55 \mu\text{m}$ and the maximum finger height $h_{f,\text{max}} = 19 \mu\text{m}$ resulting an optical aspect ratio of $AR_o = 0.21$. All screen printed structures show the typically inhomogeneity of mesh marks compared with a higher homogeneity of dispensed contacts. Pastes A and B result in similar finger geometries. Paste C presents a reduced core finger width of $w_{\text{core}} = 25 \mu\text{m}$ and a high optical aspect ratio of $AR_o = 0.46$ compared with pastes A and B.

of pastes A and B show similar finger shapes. Both pastes show a significant spreading or swelling. The achieved contact finger width is much wider than the used nozzle diameters of 30 or 25 μm , respectively. The average shading and average core finger widths of groups 9 ($w_{\text{shading,Gr.9}} = 42 \pm 3 \mu\text{m}$) and 11 ($w_{\text{shading,Gr.11}} = 52 \pm 2 \mu\text{m}$) differ significantly, even though the applied DIS process parameters were the same, and the used curing parameters were only varied in a temperature difference

of 10 °C. Potential reasons for that might be a deviation of nozzle plates or a change of paste properties during DIS.

The DIS paste C shows an improved optical aspect ratio of $AR_o = 0.46 \pm 0.02$ ($AR_{el} = 0.27 \pm 0.02$) and a reduced average core finger width of $w_{core} = 25 \pm 1 \mu m$. The applied nozzle openings and the average core finger width have the same value. The average spreading coefficient is $\xi_{spreading} = 0.62 \pm 0.03$. Consequently, the swelling phenomenon of the paste is significant. Obtaining a spreading coefficient of 1 corresponds to a contact finger shape without any spreading and minimized shading area of active area at a given grid conductivity. The homogeneity of dispensed structures is visible in the low standard deviation across all DIS groups.

4.2. Electrical Performance

Figure 4 presents the contact resistivity values $\rho_{c,TLM}$ of pastes A–C applied on CIGS substrates. On the left part of the diagram, the results of experiment 1 are shown. The contact resistivity values are classified according to the paste formulations, curing temperatures, and duration. When the average contact resistivity values are below $5 \text{ m}\Omega\text{cm}^2$, a contact formation during curing is assumed. The scattering of the measured values differs significantly depending on the applied curing conditions. If no box is shown in the diagram, the paste did not form a contact with the TCO layer at the chosen curing temperature and duration. Especially, the combination of a curing temperature below $T_c = 180^\circ\text{C}$ and a short curing time of $t_c = 5 \text{ min}$ results in no contact formation. Curing paste A at $T_c = 200^\circ\text{C}$ for $t_c = 5 \text{ min}$ results in an average contact resistivity to the TCO layer $\rho_{c,TLM} = 3.47 \pm 1.41 \text{ m}\Omega\text{cm}^2$. An average contact resistivity of $\rho_{c,TLM} = 2.11 \pm 1.07 \text{ m}\Omega\text{cm}^2$ has been reached for paste A at a curing temperature of $T_c = 190^\circ\text{C}$ and $t_c = 10 \text{ min}$. For paste B, the curing parameters of $T_c = 190^\circ\text{C}$ and $t_c = 10 \text{ min}$ also result in a contact resistivity of $\rho_{c,TLM} = 2.14 \pm 0.94 \text{ m}\Omega\text{cm}^2$. For paste C, the curing temperatures of $T_c = 200^\circ\text{C}$ and $T_c = 180^\circ\text{C}$ can result in a similar contact resistivity $\rho_{c,TLM}$, when using a different curing duration ($\rho_{c,TLM-200^\circ\text{C}} = 2.13 \pm 0.59 \text{ m}\Omega\text{cm}^2$; $\rho_{c,TLM-180^\circ\text{C}} = 2.00 \pm 0.89 \text{ m}\Omega\text{cm}^2$). The results of experiment 1 are used to choose the curing parameters for experiment 2 considering the temperature sensitive CIGS layer. The final curing parameters are shown in the experimental overview in Figure 2. Figure 4 on the right presents the contact resistivity $\rho_{c,TLM}$ results of experiment 2. All chosen curing parameters for experiment 2 show the average contact resistivity values below $5 \text{ m}\Omega\text{cm}^2$. Independent of curing parameters and printing technologies, the contact resistivity of paste A results in a range of $\rho_{c,TLM} = 2.3 \text{ m}\Omega\text{cm}^2$ and $\rho_{c,TLM} = 2.8 \text{ m}\Omega\text{cm}^2$ (groups 1–8). The dispensed metal grid of paste B, which is cured at a temperature of $T_c = 190^\circ\text{C}$ for $t_c = 10 \text{ min}$, shows a lower contact resistivity of $\rho_{c,TLM} = 0.92 \pm 0.72 \text{ m}\Omega\text{cm}^2$ compared with a curing temperature of $T_c = 180^\circ\text{C}$ for $t_c = 10 \text{ min}$ ($\rho_{c,TLM} = 1.97 \pm 0.89 \text{ m}\Omega\text{cm}^2$). Nevertheless, metal grids of paste B show lower contact resistivity values and sheet resistances than paste A, even though paste A is cured partly at higher curing temperatures. Paste C shows a contact resistivity of $\rho_{c,TLM} = 1.42 \pm 1.52 \text{ m}\Omega\text{cm}^2$.

The measurement results of the h.a.l.m. flasher IV tool are listed in **Table 1**. The CIGS modules are measured

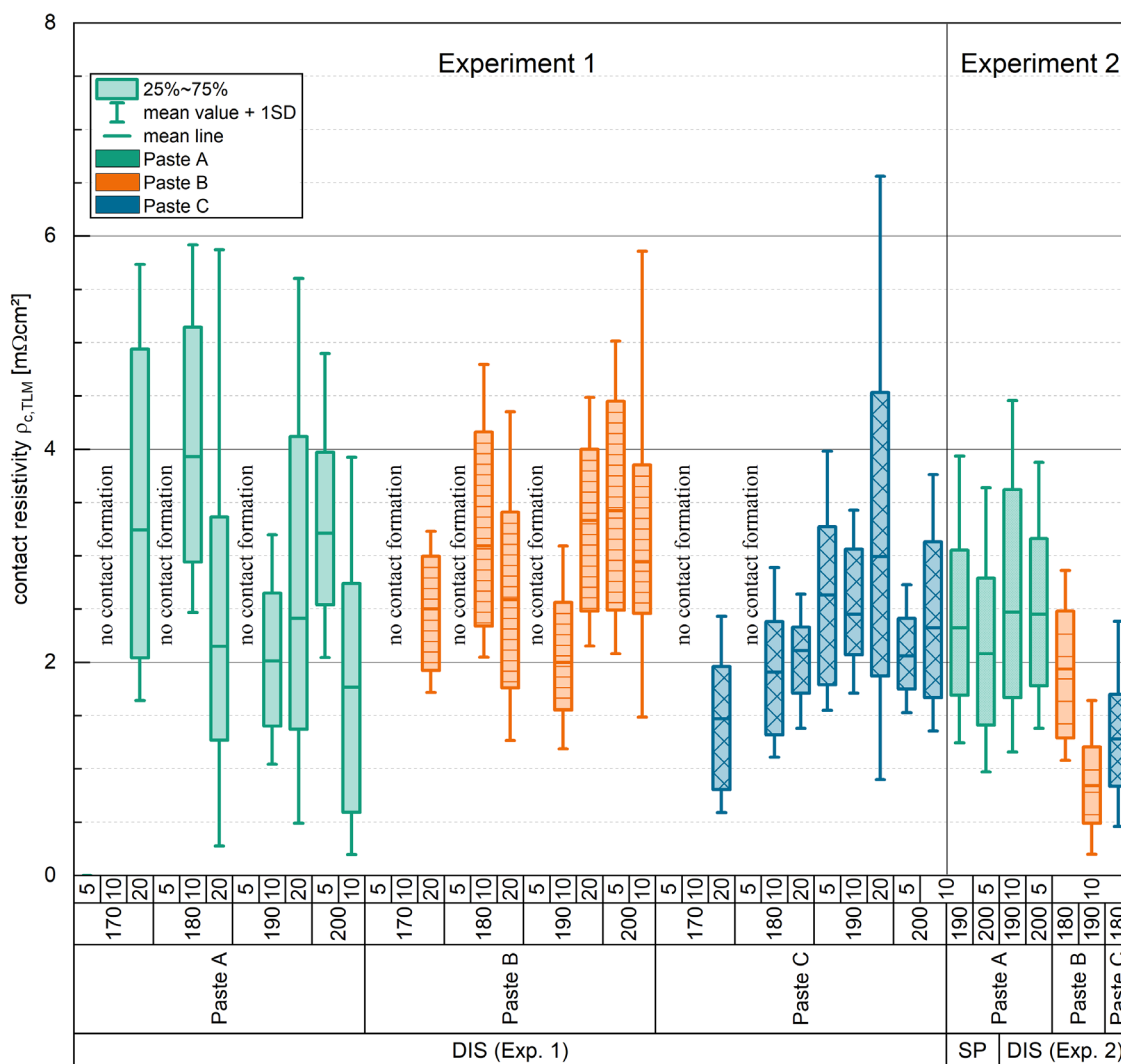


Figure 4. Contact resistivity values for the investigated low-temperature pastes A–C. The measurement procedure is described in Section 3.2.2. The contact resistivity values $\rho_{c,TLM}$ over the corresponding curing temperatures of $T_c = 170$ – 200 °C and the corresponding duration of $t_c = 5$ – 20 min are plotted (experiment 1). The curing conditions of $t_c = 5$ min at $T_c = 200$ °C as well as $t_c = 10$ min at $T_c = 190$ °C obtain promising contact resistivity values $\rho_{c,TLM}$ below 5 m Ω cm 2 for paste A. The curing duration of $t_c = 10$ min at the curing temperatures of $T_c = 180$ °C and $T_c = 190$ °C is selected for paste B for further experiments. Reasonable curing conditions of $t_c = 10$ min at $T_c = 180$ °C are chosen for paste C. The TLM results of the chosen curing conditions for each low-temperature paste are shown in the right part of the plot (experiment 2). All average contact resistivity values $\rho_{c,TLM}$ are below 5 m Ω cm 2 . On average, paste B shows the lowest contact resistivity of $\rho_{c,TLM} = 0.9 \pm 0.7$ m Ω cm 2 .

non-laminated. The grid-free CIGS mini-modules (group 1) result in an average short-circuit current density of $j_{sc,Gr,0} = 31.1 \pm 0.1$ mA cm $^{-2}$. All CIGS mini-modules with applied metal grid show obviously increased average short-circuit current density values above 31.7 mA cm $^{-2}$ with only small scattering; thereby, the dispensed metal grids as well as the screen printed metal grids achieved similar results. Group 0 shows an average FF of $FF_{Gr,0} = 67.87 \pm 3.94\%$. All CIGS samples with dispensed metal grid show an increased FF compared with group 0 except for group 6. Group 10 shows the highest average FF of the dispensed metallized samples of $FF_{Gr,10} = 71.34 \pm 1.98\%$. Especially, the FF values of groups 4 and 6 scatter significantly. A strong correlation between the increased FF and the sheet resistance cannot be identified. The reference group 0 has an

average open-circuit voltage per cell of $V_{oc,Gr,0} = 691 \pm 2$ mV, and all metallized CIGS mini-modules obtain an average open-circuit voltage per cell between $V_{oc} = 650 \pm 3$ mV and $V_{oc} = 692 \pm 6$ mV. These differences in open-circuit voltage values of the metallized CIGS-mini modules (groups 2–14) are explicable because of the used different curing conditions for the applied low-temperature pastes, resulting in temperature-based damages of the CIGS layers or diffusion processes in the CdS layer within the CIGS samples. All CIGS mini-modules with applied metal grid have increased maximum power points compared with the reference group 0 with an average maximum module power point of $P_{mmp,Gr,0} = 1.95 \pm 0.12$ W to $P_{mmp,Gr,12} = 2.05 \pm 0.11$ W for the dispensed group 12.

Table 1. Overview of the electrical performance of the investigated low-temperature pastes A–C on CIGS substrates using SP and parallel DIS. Contact resistivity $\rho_{c,TLM}$ and the contact resistance $R_{sh,TLM}$ are measured by TLM measurements (see Section 3.2.2.). The h.a.l.m. flasher IV tool is used to characterize V_{oc} , j_{sc} , P_{mpp} , and FF of the CIGS mini-modules at standard test conditions.

Paste	Group name	Curing conditions		Electrical parameters on CIGS substrates					
				$\rho_{c,TLM}$ [$m\Omega cm^2$]	$R_{sh,TLM}$ [Ωsq^{-1}]	$V_{oc}/cell$ [mV]	j_{sc} [$mA cm^{-2}$]	FF [%]	P_{mpp} [W]
Ref.	Gr. 0	–	grid-free	–	–	691 ± 2	31.1 ± 0.1	67.87 ± 3.94	1.95 ± 0.12
A	Gr. 1 Gr. 2	5 min@200 °C	SP	2.3 ± 1.3	83 ± 10	692 ± 6	31.7 ± 0.2	71.88 ± 2.6	2.01 ± 0.10
	Gr. 3 Gr. 4	10 min@190 °C	SP	2.6 ± 1.3	97 ± 9	650 ± 3	32.0 ± 0.2	69.47 ± 5.02	1.98 ± 0.16
	Gr. 5 Gr. 6	5 min@200 °C	DIS	2.6 ± 1.2	79 ± 3	656 ± 7	32.1 ± 0.1	65.67 ± 6.84	1.90 ± 0.22
	Gr. 7 Gr. 8	10 min@190 °C	DIS	2.8 ± 1.6	92 ± 12	652 ± 7	32.2 ± 0.1	69.71 ± 2.53	2.01 ± 0.09
B	Gr. 9 Gr. 10	10 min@190 °C	DIS	0.9 ± 0.7	58 ± 8	657 ± 3	31.8 ± 0.2	71.33 ± 1.98	2.04 ± 0.07
	Gr. 11 Gr. 12	10 min@180 °C	DIS	2.0 ± 0.9	64 ± 5	663 ± 4	31.7 ± 0.1	71.30 ± 3.42	2.05 ± 0.11
C	Gr. 13 Gr. 14	10 min@180 °C	DIS	1.4 ± 1.0	64 ± 6	672 ± 8	31.7 ± 0.3	68.65 ± 5.55	2.01 ± 0.18

The presented results demonstrate an advantage of applying a metallization on the TCO layer of CIGS samples by the DIS approach. Despite the difference in the contact resistivity $\rho_{c,TLM}$ or the contact finger width w , the most crucial impact seems to be the open-circuit voltage difference between the metallized groups. The results of this study indicate that a lower curing temperature and a higher aspect ratio might lead to higher open-circuit voltages. This first hypothesis needs to be verified in further experimental studies, for example, by evaluating optimized low-temperature silver pastes, which form a contact to the TCO layer at the curing temperatures below 170 °C. To date, the availability and the costs of low-temperature silver pastes with a curing temperature below 150 °C are challenging, independently of the printing process.^[8] In addition, a detailed paste characterization is required to find paste formulations with significantly reduced spreading.

5. Conclusion

For the first time, parallel DIS was applied for metallization of CIGS modules. In this study, we evaluated three different low-temperature silver pastes by DIS them through nozzle openings between 35 and 25 μm . A curing variation of these pastes was carried out for a temperature range between $T_c = 170$ °C and $T_c = 200$ °C, resulting in the average contact resistivity values $\rho_{c,TLM}$ below 5 $m\Omega cm^2$. The dispensed and screen printed metal grids on the TCO layer obtained comparable short-circuit current density and open-circuit voltage values. The front contact metallization of the CIGS mini-modules allows the use of wider cells compared with grid-free CIGS mini-modules; consequently, the cell number and the dead area of CIGS mini-modules are minimized. The homogeneity of the contact finger shape might determine the maximal possible cell width; in this case, the dispensed structures have a more effective silver consumption than screen printed metal grids. The best performing paste in this experiment shows an improved finger shape with an optical aspect ratio of $AR_o = 0.46$ and a core finger width $w_{core} = 25$ μm and a contact resistivity of $\rho_{c,TLM} = 1.4 \pm 1.0 m\Omega cm^2$ at a curing temperature of $T_c = 180$ °C. Due to the contactless printing approach and its scalability and flexibility concerning different pastes, a future prove of concept seems to be realistic. Even

without adaptation of cell width or TCO optimization, a power increase of 4.6% was already reached. Future focus of R & D should, therefore, focus on lower curing parameters and the reduction of paste spreading to minimize the shading effects of the cells.

Acknowledgements

This work was supported by the German Federal Ministry for Economic Affairs and Energy within the research project "Altura" under the contract numbers 03EE1006A and 03EE1006C. The authors were responsible for the content. Open access funding enabled and organized by Projekt DEAL.

Conflict of Interest

The authors declare no conflict of interest.

Keywords

CIGS, low-temperature pastes, solar cell metallization, thin-film photovoltaics

Received: August 11, 2020
Revised: September 25, 2020
Published online:

- [1] V. Bermudez, *Sol. Energy* **2017**, *146*, 85.
- [2] T. D. Lee, A. U. Ebong, *Renew. Sustain. Energy Rev.* **2017**, *70*, 1286.
- [3] *High-Efficient Low-Cost Photovoltaics: Recent Developments* (Eds: V. Petrova-Koch, R. Hezel, A. Goetzberger), Springer, Berlin **2019**.
- [4] G. Regmi, A. Ashok, P. Chawla, P. Semalti, S. Velumani, S. N. Sharma, H. Castaneda, *J. Mater. Sci.: Mater. Electron* **2020**, *31*, 7286.
- [5] S. Yoshida, Solar Frontier Achieves World Record Thin-Film Solar Cell Efficiency of 23.35%. http://www.solar-frontier.com/eng/news/2019/0117_press.html (accessed: June 2020).
- [6] S. Enkhart, Manz-Joint-Venture Nice Solar Energy vermeldet Wirkungsgradrekord von 17,6 Prozent für CIGS-Module, **2019**. <https://www.pv-magazine.de/2019/12/04/manz-joint-venture-nice-solar-energy-vermeldet-wirkungsgradrekord-von-17-6-prozent-fuer-cigs-module/> (accessed: January 2020).

- [7] CIGS White Paper 2019. https://cigs-pv.net/wortpresse/wp-content/uploads/2019/04/CIGS_White_Paper_2019_online.pdf (accessed: 3 February 2020).
- [8] V. Bermudez, A. Perez-Rodriguez, *Nat Energy* **2018**, 3, 466.
- [9] J. V. Li, S. Grover, M. A. Contreras, K. Ramanathan, D. Kuciauskas, R. Noufi, *Solar Energy Materials and Solar Cells* **2014**, 124, 143.
- [10] K. Kushiya, *Solar Energy Materials and Solar Cells* **2009**, 93, 1037.
- [11] D. Lee, J. Yang, Y.-S. Kim, C. B. Mo, S. Park, B. Kim, D. Kim, J. Nam, Y. Kang, *Solar Energy Materials and Solar Cells* **2016**, 149, 195 h.
- [12] M. Powalla, P. Jackson, W. Witte, D. Hariskos, S. Paetel, C. Tschamber, W. Wischmann, *Sol. Energy Mater. Sol. Cells* **2013**, 119, 51.
- [13] K. Thalheimer, US patent, US4758526A, **1988**.
- [14] A. E. Delahoy, S. Y. Guo, C. Paduraru, A. Belkind, *J. Vac. Sci. Technol. A: Vac. Surf. Films* **2004**, 22, 1697.
- [15] A. E. Delahoy, L. Chen, M. Akhtar, B. Sang, S. Guo, *Sol. Energy* **2004**, 77, 785.
- [16] P. Gondoni, *Dissertation*, Politecnico di Milano, Mailand **2014**.
- [17] M. F. A. M. van Hest, M. S. Dabney, J. D. Perkins, D. S. Ginley, M. P. Taylor, *Appl. Phys. Lett.* **2005**, 87, 32111.
- [18] Y. Hirai, Y. Kurokawa, A. Yamada, *Jpn. J. Appl. Phys.* **2014**, 53, 12301.
- [19] A. Illiberi, B. Kniknie, J. van Deelen, H. L. A. H. Steijvers, D. Habets, P. J. P. M. Simons, A. C. Janssen, E. H. A. Beckers, *Sol. Energy Mater. Sol. Cells* **2011**, 95, 1955.
- [20] S. Siebentritt, U. Rau, *Wide-Gap Chalcopyrites*, Springer Verlag, Berlin **2006**.
- [21] M. Edoff, *Ambio* **2012**, 41, 112.
- [22] O. Lundberg, E. Wallin, V. Gusak, S. Sodergren, S. Chen, S. Lotfi, F. Chalvet, U. Malm, N. Kaihovirta, P. Mende, G. Jaschke, P. Kratzert, J. Joel, M. Skupinski, P. Lindberg, T. Jarmar, J. Lundberg, J. Mathiasson, L. Stolt, in *IEEE 43rd Photovoltaic Specialists Conf.*, **2016**, pp. 1293–1296.
- [23] A. Chirilă, P. Reinhard, F. Pianezzi, P. Bloesch, A. R. Uhl, C. Fella, L. Kranz, D. Keller, C. Gretener, H. Hagendorfer, D. Jaeger, R. Erni, S. Nishiwaki, S. Buecheler, A. N. Tiwari, *Nat. Mater.* **2013**, 12, 1107.
- [24] E. Fortunato, D. Ginley, H. Hosono, D. C. Paine, *MRS Bull.* **2007**, 32, 242.
- [25] B. Retterstol Olaisen, S. Woldegiorgis, P.-O. Westin, M. Edoff, L. Stolt, A. Holt, E. Stenrud, Presented at *Technical Digest of the 15th International Photovoltaic Science and Engineering Conf.*, Shanghai, China **2005**.
- [26] P. A. Hersh, C. J. Curtis, M. F. A. M. van Hest, J. J. Kreuder, R. Pasquarelli, A. Miedaner, D. S. Ginley, *Prog. Photovolt: Res. Appl.* **2011**, 19, 973.
- [27] J. D. Fields, M. S. Dabney, V. P. Bollinger, M. F. A. M. van Hest, in *IEEE 40th Photovoltaic Specialist Conf.*, **2014**, pp. 162–165.
- [28] J. D. Fields, G. Pach, K. A. W. Horowitz, T. R. Stockert, M. Woodhouse, M. F. A. M. van Hest, *Sol. Energy Mater. Sol. Cells* **2017**, 159, 536.
- [29] J. van Deelen, C. Frijters, *Sol. Energy* **2017**, 143, 93.
- [30] N. Cavallari, F. Pattini, S. Rampino, F. Annoni, M. Barozzi, M. Bronzoni, E. Gilioli, E. Gombia, C. Maragliano, M. Mazzer, G. Peponi, G. Spaggiari, R. Fornari, *Appl. Surf. Sci.* **2017**, 412, 52.
- [31] M. L. Crozier, P. Adamson, A. Brunton, S. Henley, J. D. Shephard, G. Kartopu, S. Irvine, P. M. Kaminski, J. M. Walls, *IEEE 40th Photovoltaic Specialist Conf.*, **2014**, pp. 2784–2788.
- [32] E. Markauskas, P. Gečys, A. Žemaitis, M. Gedvilas, G. Račiukaitis, *Sol. Energy* **2015**, 120, 35.
- [33] S. Nishiwaki, A. Burn, S. Buecheler, M. Murali, S. Pilz, V. Romano, R. Witte, L. Krainer, G. J. Spühler, A. N. Tiwari, *Prog. Photovolt: Res. Appl.* **2015**, 23, 1908.
- [34] M. Pospischil, T. Riebe, A. Jimenez, M. Kuchler, S. Tepner, T. Geipel, D. Ourinson, T. Fellmeth, M. Breitenbücher, T. Buck, M. Dhamrin, F. Clement, *AIP Conf. Proc.* **2019**, 2156, 20005.
- [35] M. Pospischil, M. Kuchler, M. Klawitter, C. Rodríguez, M. Padilla, R. Efinger, M. Linse, A. Padilla, H. Gentischer, M. König, M. Horteis, L. Wende, O. Doll, R. Zengerle, F. Clement, D. Biro, *Energy Proc.* **2015**, 67, 138.
- [36] M. Pospischil, Dissertation, Albert-Ludwigs-Universität, Freiburg im Breisgau, **2016**.
- [37] S. Tepner, L. Ney, M. Linse, A. Lorenz, M. Pospischil, K. Masuri, F. Clement, *Prog Photovolt Res Appl* **2020**, 28, 1054.
- [38] A. Lorenz, M. Linse, H. Frintrup, M. Jeitöe, A. Mette, M. Lehner, R. Greutmann, H. Brocker, M. König, D. Erath, F. Clement, in *Proc. 35th Eur. Photovolt. Sol. Energy Conf. Exhib.* **2018**.
- [39] VDMA Photovoltaics Equipment, *International Technology Roadmap for Photovoltaics (ITRPV): Eleventh Edition*, **2020**.
- [40] S. Tepner, N. Wengenmeyr, L. Ney, M. Linse, M. Pospischil, F. Clement, *Sol. Energy Mater. Sol. Cells* **2019**, 200, 109969.
- [41] F. Clement, M. Linse, S. Tepner, N. Wengenmeyr, L. Ney, K. Krieg, A. Lorenz, M. Pospischil, S. Bechmann, K. Oehle, S. Steckemetz, R. Preu, in *Proc. 36th Eur. Photovolt. Sol. Energy Conf. Exhib.* **2019**, pp. 255–258.
- [42] M. Pospischil, M. Klawitter, M. Kuchler, J. Specht, H. Gentischer, R. Efinger, C. Kroner, M. Luegmair, M. König, M. Horteis, C. Mohr, L. Wende, J. Lossen, M. Weib, O. Doll, I. Koehler, R. Zengerle, F. Clement, D. Biro, *Energy Proc.* **2013**, 43, 111.
- [43] M. Pospischil, M. Kuchler, M. Klawitter, I. Lacmago Lontchi, S. Tepner, R. Efinger, M. Linse, D. Witt, S. Gutscher, A. Brand, M. König, L. Wende, F. Clement, D. Biro, in *Proc. 32nd Eur. Photovolt. Sol. Energy Conf. Exhib.* **2016**.
- [44] D. Biro, J. Specht, D. Scheffler, M. Pospischil, F. Clement EP 2 612 350 B1, **2013**.
- [45] M. Pospischil, H. Gentischer, M. Kuchler, M. Klawitter, F. Clement, D. Biro, J. Specht EP 3 068 626 B1, **2016**.
- [46] HighLine Technology GmbH. <https://highline-technology.com/> (accessed: August 2020).
- [47] M. A. Skylar-Scott, J. Mueller, C. W. Visser, J. A. Lewis, *Nature* **2019**, 575, 330.
- [48] M. Pospischil, J. Specht, M. König, M. Horteis, C. Mohr, F. Clement, D. Biro, *IEEE J. Photovolt.* **2014**, 4, 498.
- [49] J.-H. Yoon, J.-K. Park, W. M. Kim, J. Lee, H. Pak, J.-H. Jeong, *Sci Rep* **2015**, 5, 1107.
- [50] K. L. Chopra, P. D. Paulson, V. Dutta, *Prog. Photovolt: Res. Appl.* **2004**, 12, 69.
- [51] T. Strauch, M. Demant, A. Lorenz, J. Haunschild, S. Rein, in *Proc. 29th Eur. Photovolt. Sol. Energy Conf. Exhib* **2014**, pp. 1132–1137.
- [52] S. Tepner, N. Wengenmeyr, M. Linse, A. Lorenz, M. Pospischil, F. Clement, *Adv. Mater. Technolog.* **2020**, 2000654.
- [53] S. Tepner, L. Ney, M. Linse, A. Lorenz, M. Pospischil, K. Masuri, F. Clement, *Advances in Screen Printed Metallization for Si-Solar Cells – Towards Ultra-fine Line Contact Fingers Below 20 μm*. <https://doi.org/10.13140/RG.2.2.33088.69126>.